Journal of Power Sources 446 (2020) 227298

Contents lists available at ScienceDirect

Journal of Power Sources

journal homepage: www.elsevier.com/locate/jpowsour

Dual interface coupled molybdenum diselenide for high-performance sodium ion batteries and capacitors

Xu Zhao [a,d,e,*], Yundong Zhao [e], Bin Huang [b,d], Zhijian Yang [a], Wei Cai [e], Jiehe Sui [e], Guozhong Cao [d,**], Hong-En Wang [c,d,***]

[a] *Institute of Chemical Materials, China Academy of Engineering Physics, Mianyang, 621900, China*
[b] *College of Chemistry and Bioengineering, Guilin University of Technology, Guilin, Guangxi, 541004, China*
[c] *State Key Laboratory of Advanced Technology for Materials Synthesis and Processing, Wuhan University of Technology, Wuhan, 430070, China*
[d] *Department of Materials Science and Engineering, Clean Energy Institute, University of Washington, Seattle, 98195, WA, USA*
[e] *School of Materials Science and Engineering, Harbin Institute of Technology, Harbin, 150001, China*

HIGHLIGHTS

- An interfacial coupling strategy has been promoted using MoO_2 and graphene.
- MoO_2 and graphene facilitated electron transport in $MoSe_2$.
- A sodium ion capacitor based on $MoO_2@MoSe_2$/graphene has been assembled.
- Device in this paper achieved high energy density and excellent power output.

GRAPHICAL ABSTRACT

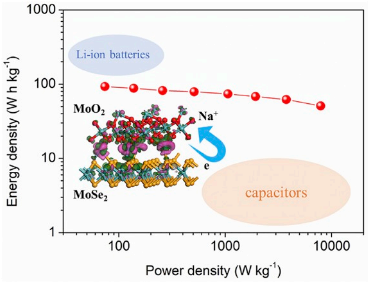

ARTICLE INFO

Keywords:
Dual interfacial coupling
$MoO_2@MoSe_2$/Graphene
DFT simulations
Sodium ion capacitors

ABSTRACT

Sodium ion capacitors (SICs) can combine the merits of electrochemical capacitors and batteries. The present paper reports a dual-interface composite consisting of few-layer $MoSe_2$ vertically anchored on reduced graphene oxide followed by decoration with metallic MoO_2 nanoparticles ($MoO_2@MoSe_2$/rGO) as anode material for SICs. Enhanced sodium-ion diffusion and electron transfer could be attributable not only to the metallic MoO_2 and graphene, but also to the electronic coupling of MoO_2 and $MoSe_2$ at interface, which has been verified and corroborated with DFT simulations and EIS analyses. $MoO_2@MoSe_2$/rGO electrode delivers a high sodium-ion storage capacity of 394 mAh g^{-1} at 3.2 A g^{-1} and no obvious capacity degradation for over 5000 cycles at 5 A g^{-1}. When paired with an activated carbon cathode, a SIC has been successfully fabricated, manifesting a high energy density of 51 W h kg^{-1} at 7920 W kg^{-1} as well as long cyclability (>97% of capacity retention at 10 A g^{-1} over 4500 cycles). The synergistical dual-interface modification strategy proposed here can pave a way to the rational design and fabrication of a broad array of composite electrodes for next-generation Na-ion batteries and capacitors in clean energy technologies.

---

[*] Corresponding author. Institute of Chemical Materials, China Academy of Engineering Physics, Mianyang, 621900, China.

[**] Corresponding author. Department of Materials Science and Engineering, Clean Energy institute, University of Washington, Seattle, 98195, WA, USA.

[***] Corresponding author. State Key Laboratory of Advanced Technology for Materials Synthesis and Processing, Wuhan University of Technology, Wuhan, 430070, China.

E-mail addresses: xuzhao@caep.cn (X. Zhao), gzcao@u.washington.edu (G. Cao), hongenwang@whut.edu.cn (H.-E. Wang).

https://doi.org/10.1016/j.jpowsour.2019.227298
Received 6 July 2019; Received in revised form 30 August 2019; Accepted 11 October 2019
Available online 26 October 2019

1. Introduction

With the ever-expanding demands for energy and intense appeal for reducing carbon dioxide emission, the innovation of novel energy storage devices, such as supercapacitors and secondary batteries has received worldwide attention in the past few decades [1]. Among various possible candidates, lithium-ion batteries (LIBs) have dominated the market share since commercialization. However, there is a critical concern about the limited Li resources in the earth crust, which inspires us to explore promising alternative battery techniques using naturally abundant elements. Metallic sodium processes similar physical/chemical properties with that of lithium. Sodium is the fourth most abundant element on earth, providing a compelling rationale for the development of sodium ion batteries (SIBs) to be used as alternatives to LIBs [2]. The electrode selection and the electrical storage mechanism of SIBs and LIBs are basically similar except for ion carriers. In terms of cathode materials, the intercalation chemistry of sodium is very similar to that of lithium, making it possible to use similar compounds for both systems. However, there are some obvious differences between these systems when comes to the anode materials. Na-ions (1.02 Å) are larger compared to Li-ions (0.76 Å), which affects the phase stability, transport properties and interphase formation of an anode material [3,4]. Particularly, sodium ion capacitors (SICs) have received increasing interests due to the similar electrochemistry and unique merits of sodium. Particularly, SICs can combine Na-ion battery-type anodes and capacitor-type cathodes in a Na-salt containing organic electrolyte, offering a high energy density without compromising the high power or cycle life, which have attached much attentions recently [5,6]. Nonetheless, development of SIBs and SICs with high-rate capability and long lifespan remains elusive mainly due to the sluggish reaction kinetics stemmed from larger sodium ion radius (0.102 nm for Na^+ *vs.* 0.076 nm for Li^+) [7]. For instance, carbon has been widely used in LIBs for decades due to its low cost and high stability, but the low specific capacities and small interlayer distance of graphite restrict its further applications as anode in SIBs. The metallic nanomaterials (Sn, Sb, et al.) merits on the high electrical conductivity, however, the poor cycling stability was restricted by the large volume changes during charge/discharge process. Therefore, developing a new anode material for electrochemical Na-ion storage has become a promising research topic.

Recently, interfacial coupling has provided a clear direction for searching potential anodes for SIBs and SICs. By tailoring the chemical properties of the two components, constructing heterostructures endows hybrids with diverse functions due to the tunable physicochemical properties and interfacial interactions, exhibiting enhanced electrochemical performances in SIBs. For instance, Li et al. reported a bimetal sulfide electrode for high rate SIBs using the synergistic interfacial effect at N/S doped graphene [8]. Benefiting from interfacial coupling effects, MoS_2 hybrid with S-doped graphene showed outstanding cycling stability and high-rate performance in both LIBs and SIBs [9,10]. Increasing attentions have been focused on $MoSe_2$ as a potential anode for SIBs due to its larger interlayer spacing (0.67 nm) [11] than other transition metal chalcogenides like VS_x, which may be suitable for fast and reversible sodium-ion storage with high specific capacities. However, the electronic conductivity and structure stability of $MoSe_2$ electrode still need further improvement for practical application. Hybridization with carbon nanomaterials [12] can be a promising strategy to improve the electrical conductivity of $MoSe_2$. However, either the inhomogeneous distribution of the respective components and poor contact at interface of $MoSe_2$ and conductive matrix, or expensive synthetic route may undermine the electron transport and charge transport at $MoSe_2$/C interface, leading to limited improvement of electrochemical properties.

To address these issues, we herein report the designed synthesis of a novel heterostructure nanocomposite comprised of MoO_2 nanoparticles and graphene co-modified few-layered (named as MoO_2@$MoSe_2$/rGO). $MoSe_2$ nanolayers with exposed (002) facets were firstly grown on graphene *via* a surfactant-assisted hydrothermal reaction. Then, metallic MoO_2 nanoparticles were decorated on the $MoSe_2$ surface to further enhance the electrical conductivity of $MoSe_2$. The ultrathin $MoSe_2$ sheets can afford abundant active sites for electrolyte permeation and wetting on the electrode surface. When tested as an anode in Na-half cells, the composite material delivers a superior rate capacity of 394 mA h g^{-1} at a high current density of 3.2 A g^{-1}. Kinetics analysis further elucidates pseudocapacitive Na^+ ion storage dominated in such a heterostructure anode. DFT simulations suggest that a metallic nature of MoO_2@$MoSe_2$/rGO and a charge accumulation at MoO_2 and $MoSe_2$ interface, enabling a fast electron/ion diffusion network in the hybrid. Moreover, coupling with an activated carbon (AC) cathode, the as-assembled Na-ion capacitor (SIC) exhibits an energy density of 52 Wh kg^{-1} at a power density of 7920 W kg^{-1}, and long lifespan of 4500 cycles at 10 A g^{-1} with nearly 100% of capacitance retention, which is very competitive compared to those SICs reported in literature.

2. Experimental section

Materials Synthesis: All chemicals were of analytical grade and used as received without further purification.

Synthesis of Se-precursor: Se powders (0.158 g, 99.99%, Aladdin) were dissolved in 10 mL N_2H_4 solution (98%, Alfa-Aesar) with stirring in a sealed beaker under dark for 24 h at room temperature.

Synthesis of GO precursor: Cetyltrimethyl ammonium bromide (CTAB, 0.3 g, 98%, Alfa-Aesar) were dissolved in 15 mL graphene oxide solution (GO, 2 mg/mL) under stirring at room temperature.

Synthesis of $MoSe_2$/rGO: $Na_2MoO_4 \cdot 2H_2O$ (0.242 g, 99%, Aladdin) were dissolved into 20 mL deionized water and poured into GO precursor. After stirring for 2 h, Se-precursor was added dropwise. Then, the resultant mixture was transferred into a 50 mL Teflon-lined stainless-steel autoclave with capacity, sealed and heated at 200 °C for 12 h. After reaction, the autoclave was cooled to room temperature naturally. The precipitate was collected by centrifugation and washed with deionized water at least four times. Finally, the as-obtained products were dispersed in 20 mL deionized water.

Synthesis of MoO_2@$MoSe_2$/rGO: MoO_2 nanoparticles were loaded on the $MoSe_2$/rGO through a solvothermal reaction referringTypically, 0.15 g of MoO_3 powder (99%, Aladdin) and 10 mL ethylene glycol (99%, Alfa-Aesar) were added into 20 mL $MoSe_2$/rGO aqueous solution under sonication for 1 h. The mixture was then transferred into a 50 mL autoclave with a PTFE-liner, sealed and heated at 200 °C for 24 h. The resultant black powders were rinsed with deionized water and ethanol several times and then dried under vacuum.

Materials characterizations: The crystal structure of the samples was characterized by X-ray diffraction (XRD) measurements (PANalytical X'Pert Pro X-ray diffractometer). The morphology and microstructure were characterized directly by transmission electron microscope (TEM, FEI Tecnai G2 F30 with a working voltage of 200 kV). The surface elemental composition and chemical state were analyzed by X-ray photoelectron spectroscope (XPS, Thermo Fisher Scientific ESCALAB 250-Xi) with Al Kα radiation.

Electrochemical measurements: Electrochemical tests were performed using 2032-type coin cells at room temperature. The coin cells were assembled in a Braun glovebox purged with Ar with O_2 and H_2O contents below 0.5 ppm. The working electrode was prepared by mixing the active materials (80 *wt* %), carbon black (Super-P, 10 *wt* %), and poly-vinylidene fluoride (PVDF, 10 *wt* %) in N-methyl-2-pyrrolidone (NMP) solvent. The resulting slurry was coated on a Cu foil and dried at 70 °C in vacuum. 1 M $NaClO_4$ dissolved in ethylene carbonate/diethyl carbonate (EC/DEC = 1:1 *vol* %) with 5% fluoroethylene carbonate (FEC) additive was used as electrolyte, and fresh sodium pieces as the counter/reference electrode, glass fiber (Whatman GF/D) as the separator. Cyclic voltammetry (CV) was recorded on a CHI–650B electrochemical workstation within a potential window of 0.01–3.0 V vs. Na^+/Na at a scan rate of 0.2 mV s^{-1}. Galvanostatic charge-discharge (GCD) tests were carried out on a Land-CT-2001A battery tester at various current densities. Electrochemical impedance spectra (EIS) were measured at open-circuit potential on an Autolab PGSTAT-302 N electrochemical workstation in the frequency range from of 0.01 Hz–100 kHz with an amplitude of 5 mV.

Hybrid sodium ion capacitors (SICs) were fabricated using commercial activated carbon (purchased from Nanjing Xianfeng Nano., coated on Al foil) as cathode and MoO_2@$MoSe_2$/rGO as anode. Before assembling, the anode was pre-cycled in a half-cell for three cycles in 1–3 V and sodiated to 1.0 V in the 4th cycle. The specific energy and specific power densities of Na-ion capacitors were calculated as follows:

$$\mathrm{E} = (t2 - t1)$$

$$\mathrm{P} = \frac{E}{t} = \Delta V \frac{I}{m}$$

$$\Delta \mathrm{V} = V_{max} - V_{min}$$

where E (Wh kg^{-1}) is energy density, P (W kg^{-1}) is power density, I is the constant current (A), t_1 and t_2 is the start time and end time in the discharge process, $V_{\max}$ is the potential at the beginning of discharge after the IR drop, $V_{\min}$ is the cut-off voltage in the discharge process. The energy density and power density of HSICs against the two electrodes in device were calculated based on the total mass of the active materials of anode and cathode.

DFT simulations: The Cambridge Serial Total Energy Package (CASTEP) with ultra-soft pseudopotentials was employed in density functional theory (DFT) simulations. The energy cutoff for the plane-wave expansion was set to 400 eV. The exchange-correlation effects were described by the generalized gradient approximation with the Perdew-Burke-Ernzerhof functional (PBE). The Brillouin zone integration was sampled with a Monkhorst-Pack grid of $3 \times 2 \times 1$ special k-point meshes for geometry optimization of MoO_2, $MoSe_2$ and MoO_2@$MoSe_2$ hybrids. Moreover, the Van-der Walls force effect is also considered to describe the layered structure of $MoSe_2$. The vacuum between slabs is ~15 Å to avoid the unnecessary interaction between neighboring slabs. All the atoms are allowed to be fully relaxed until Hellmann-Feynman forces on each atom were smaller than 0.04 eV $Å^{-1}$, and spin-polarization was considered during the calculations.

3. Results and discussion

The MoO_2@$MoSe_2$/rGO nanocomposite was prepared and detailed route was listed in experimental section and Scheme 1. First, ultrathin $MoSe_2$ nanosheets were vertically grown on the rGO by a surfactant-mediated hydrothermal process using cetyl trimethyl ammonium bromide (CTAB). Briefly, the negatively charged GO surface was modified by positively charged CTAB, which could adsorb the Mo-anions through electrostatic interaction, facile a vertical align of $MoSe_2$ nanosheets and rGO substrates [13]. In the following solvothermal process, ethylene glycol (EG) can reduce MoO_3 into MoO_2 nanoparticles that can be in situ decorated on the $MoSe_2$ surface. The formation of such a MoO_2@$MoSe_2$/rGO heterostructure was mainly due to the synergy between various components: (1) few-layered $MoSe_2$ nanosheets can afford a high surface for MoO_2 nucleation and growth into nanoparticles with homogeneous dispersion and less aggregation; (2) deposition of MoO_2 nanoparticles on $MoSe_2$ surface can also avoid the undesired restacking of $MoSe_2$ nanosheets.

The crystal structure of the as-obtained product was firstly studied by powder X-ray diffraction (XRD) pattern as shown in Fig. 1a. The diffraction peaks at 31.4°, 34.4°, 55.9° and 65.6° can be readily assigned to (100), (102), (110) and (200) crystal planes of hexagonal $MoSe_2$ (JCPDS card No. 29–0914). The nearly absent (002) peak at $2\theta = 13.7°$ indicates the formation of few-layered $MoSe_2$ nanosheets. In contrast, the (002) peak can be noted in bare $MoSe_2$ and MoO_2@$MoSe_2$, indicating the multi-layered $MoSe_2$ structure (Fig. S1). Some other peaks at 26.0°, 36.9°, 41.6° and 53.4° can be well indexed to orthorhombic MoO_2 (JCPDS card No. 65–5787). No diffraction peaks for other Mo-oxides phases are detected. The broadened peaks of MoO_2 indicate its small crystallite size [14]. The surface element composition and chemical valence states of the elements were investigated by X-ray photoelectron spectroscopy (XPS) analyses. The survey spectrum confirms the major signals from Mo, Se, C and O elements (Fig. S2), indicating the high purity of the composite sample. Fig. 1b displays the high resolution XPS spectra of Mo-3d. After deconvolution, the asymmetric shape of Mo 3d bands can be separated into several sets of valence states. One pair of bands centered at 231.6 eV and 228.4 eV can be indexed to the spin-orbital splitting components of $3d_{3/2}$ and $3d_{5/2}$ of Mo^{4+} in $MoSe_2$ [15]. Another pair of bands at 233.4 eV and 230.3 eV can be indexed to the $3d_{3/2}$ and $3d_{5/2}$ of Mo^{4+} in MoO_2 [16]. The bands at high binding energy of about 235 can be assigned to the Mo^{6+}, which could be caused by the slight surface oxidation [17]. Besides, two minor peaks at 228.4/229.7 eV are attributable to the formation of Mo–C bonding at $MoSe_2$ and graphene interface, acting as a bridge of electron and Na-ion transfer through the electrodes freely [18]. The high-resolution Se 3d XPS spectrum (Fig. 1c) with two bands centered at 54.2 eV and 55.1 eV correspond to the Mo–Se bonds in $MoSe_2$. The deconvolution of C 1s XPS spectrum (Fig. 1d) indicates the existence of several bands at 284.8 eV (C–C), 285.6 eV (C–O) and 282.3 eV (C–Mo). The anti-aggregation characteristics of the MoO_2@$MoSe_2$ heterostructure anchored on rGO can endow the composite material a high specific surface area as confirmed by nitrogen adsorption/desorption isotherms test (Fig. S3). The small hysteresis in the P/P_0 range of 0.5–0.9 indicates the presence of mesopores in the sample. The calculated specific surface area and pore volume are 151.2 $m^2\,g^{-1}$ and 0.54 $cm^3\,g^{-1}$, respectively. The carbon content can be simply calculated (~4%) and tested through a thermogravimetric analysis (TGA) technique (Fig. S4). Low carbon

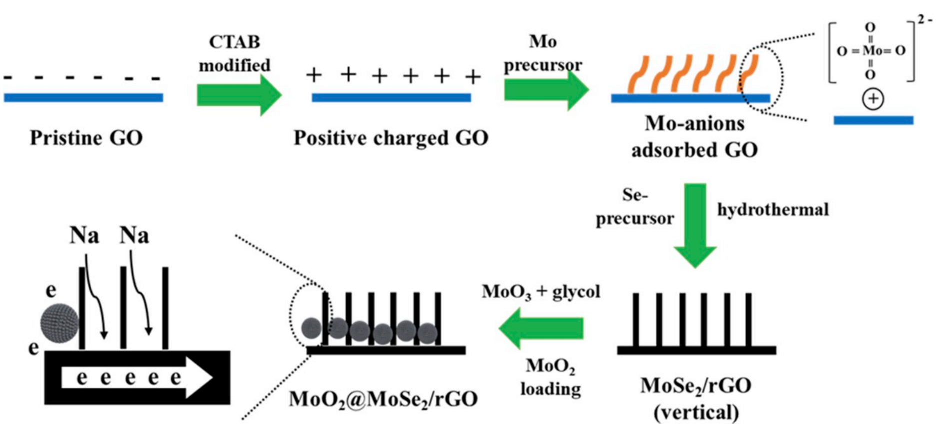

Scheme 1. Schematic illustration for the synthesis of MoO_2@$MoSe_2$/rGO heterostructure.

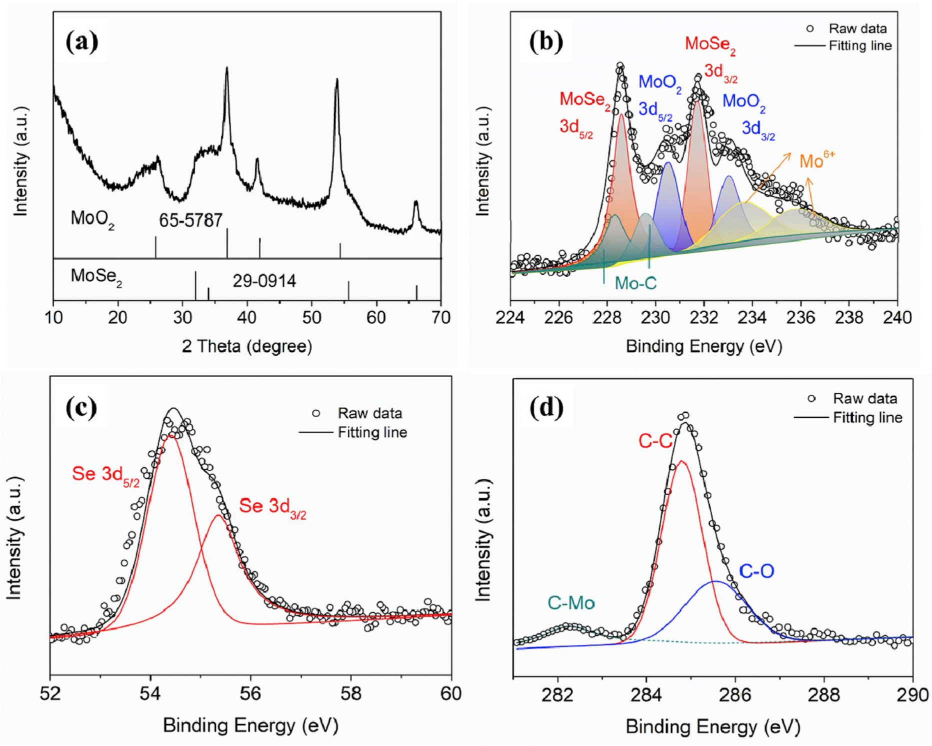

Fig. 1. (a) XRD pattern of MoO_2@$MoSe_2$/rGO heterostructure; High resolution XPS spectra of (b) Mo 3d, (c) Se 3d and (d) C 1s.

content could be positive to the usage of active materials. The relative mass ratio between MoO_2 and $MoSe_2$ can be calculated to be 1:2 using the chemical reactions listed in supporting information. The lower crystallinity of $MoSe_2$ might explain the low intensity of XRD peaks.

More details of microstructure of the MoO_2@$MoSe_2$/rGO product was observed through TEM. Fig. 2a shows abundant few-layered $MoSe_2$ nanoarrays dispersed on the surface of graphene nanosheets without obvious aggregation. In addition, cluster-like MoO_2 nanoparticles are attached to the $MoSe_2$ sheets. Selected-area electron diffraction (SAED) pattern in Fig. 2b reveals the coexistence of diffraction rings that can be well indexed to (200), (100) of $MoSe_2$ (JCPDS No. 29–0914) and (−311), (−211), (011) of MoO_2 (JCPDS No. 65–5787). The diffraction peak assigned to graphene could not be easily distinguished, indicating a single layered structure or amorphous state. In the HRTEM image (Fig. 2c), most $MoSe_2$ sheets possess few-layered feature. In addition, MoO_2 nanocrystals with diameters 5–8 nm that are attached on the $MoSe_2$ sheets tightly, forming coherent MoO_2–$MoSe_2$ heterojunctions on nanoscale. Further, detailed microstructure of as-loaded MoO_2 nanoparticles could be achieved through inverse Fast Fourier Transform (IFFT) pattern, as shown in Fig. 2d. Compared with the HRTEM image, the IFFT image with plane fringes shows much more clearly bands of 0.34 nm (Fig. 2e), which correspond to the (011) facet of MoO_2 [19]. Both of $MoSe_2$ and graphene keeps the few-layered structure, implying a confined growth process during the hydro- and solvo-thermal reaction.

The nanostructured $MoSe_2$ and MoO_2 are beneficial for fast sodiation/desodiation kinetics with very short Na^+ diffusion lengths. In addition, the metallic MoO_2 can boost the electron transport and the MoO_2@$MoSe_2$ heterojunction can facilitate charge transfer at its interface. The morphologies and microstructures of a series of controlled samples were also shown in supporting information Figs. S5–6 for comparison. Detailed discussions are summarized in the supporting information.

The electrochemical properties of MoO_2@$MoSe_2$/rGO heterostructure were firstly evaluated in coin-type Na-half cells using cyclic voltammetry (CV) method (Fig. 3a). The sweep reveals the composite electrode experiences a multistep redox reaction. During the first cathodic scan, a broad peak at 1.2–1.0 V corresponds to the Na-ion intercalation into the MoO_2 and $MoSe_2$ lattice [20]. Another broad peak at low voltage region (<0.5 V) signifies the formation of solid-electrolyte interphase (SEI) film and conversion reaction of $MoSe_2$ [21]. During the first anodic scan, a small peak at about 1.53 V and a main peak at about 1.8 V corresponds to the stepwise desodiation of MoO_2 and the restoration of original $MoSe_2$. In addition, the rough overlapping of the CV curves in the 2nd and 3rd cycles demonstrate the Na-ion insertion/extraction into/from the composite electrode is highly reversible. Fig. 3b compares the 3rd cycle of CV curves of MoO_2@$MoSe_2$/rGO composite electrode with several controlled samples. Clearly, the MoO_2@$MoSe_2$/rGO electrode displays the highest current response after active mass calibration, suggesting the highest Na-ion storage capability. Fig. 3c shows the voltage hysteresis (overpotential) between the redox peaks of all the electrodes, demonstrating that the MoO_2@$MoSe_2$/rGO electrode exhibits the best reaction kinetics with lowest polarization (0.23 V), indicating a lowest sodium ion diffusion barrier. Fig. 3d presents the galvanostatic discharge/charge (GCD) curves of the MoO_2@$MoSe_2$/rGO electrode measured at a current density of 0.1 A g^{-1}. The composite electrode displays a high discharge/charge capacity of 606/524 mA h g^{-1} at 0.1 A g^{-1} with a high Coulombic efficiency (CE) of 86%, which is much higher than those of all other controlled samples including bare $MoSe_2$ and MoO_2. The initial irreversible capacity loss can be mainly ascribed to the electrolyte decomposition accompanied by the formation of a SEI film [22]. After full activation, the CE quickly rises to 95% and 97% in the 2nd and 3rd cycle. The rate performances are shown in Fig. 3e. The MoO_2@$MoSe_2$/rGO electrode exhibits a much higher rate capacities of 515, 503, 481, 440, 415 and 394 mA h g^{-1} at 0.1, 0.2, 0.4, 0.8, 1.6 and 3.2 A g^{-1} respectively, higher than those of $MoSe_2$, MoO_2@$MoSe_2$ and $MoSe_2$/rGO counterparts. A charge capacity of 519 mA h g^{-1} can be recovered when the current density is suddenly switched back to 0.1 A g $^{-1}$ again, which shows its superior electrode stability. The GCD curves of MoO_2@$MoSe_2$/rGO at various current densities are exhibited in Fig. 3f. All the GCD curves show similar sloping curves with small deviation, evidencing the low overpotential during Na-ion insertion/extraction processes. A high

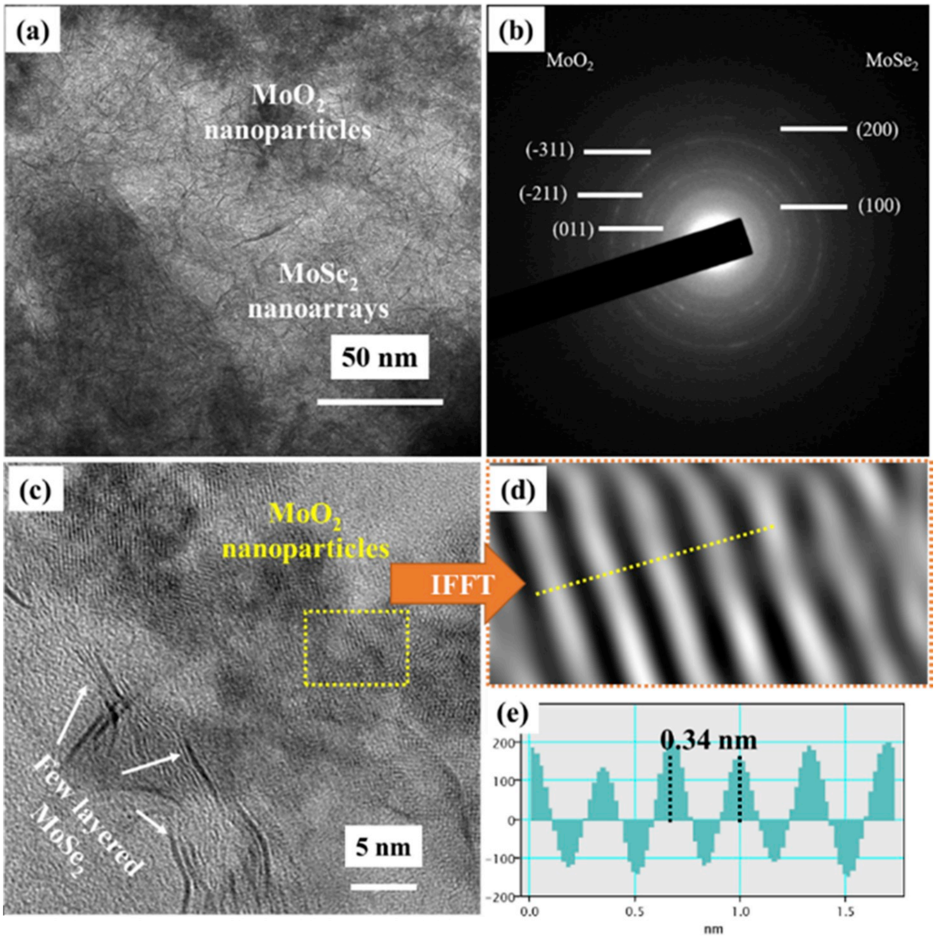

Figure 2. (a) TEM image, (b) SAED pattern and (c) HRTEM of $MoO_2@MoSe_2$/rGO heterostructure. (d) Inverse Fast Fourier transform patterns of selected yellow area in (c). (e) The linear profile obtained from the inset yellow line in (d), showing a lattice of 0.34 nm.

capacity retention of 76.5% could be achieved when the current density increases from 0.1 to 3.2 A g^{-1}, indicating its excellent rate capability. Even cycling at a high current density of 5 A g^{-1}, the as-prepared $MoO_2@MoSe_2$/rGO electrode still exhibits an excellent stability over 5000 cycles (Fig. 3g). The impressive electrochemical performance at high current densities could be attributed to the rapid Na-ion diffusion and electron transport within the heterostructure: (1) rGO and metallic MoO_2 could act as a dual electronic transport pathway to enhance the electronic conductivity of as-prepared $MoO_2@MoSe_2$/rGO hybrids; (2) sodium ion diffusion can be boosted by ultrasmall MoO_2 nanoparticles and few-layered $MoSe_2$; (3) Space between adjacent few layer $MoSe_2$ may be the buffer space for volume changes.

Electrochemical impedance spectra (EIS) of the three electrodes after rate property tests were recorded to further probe the electrode kinetics. In Fig. 4a, all the EIS curves contain a semi-circle at high-frequency region and a sloping line at low frequency domain. The semicircle and sloping line correspond to the charge transfer process at electrode/electrolyte interface and Na$^+$ diffusion in the solid electrode, respectively. Evidently, $MoO_2@MoSe_2$/rGO heterostructure possesses the lowest charge-transfer resistance and embraces the advantage of fastest kinetics for sodiation/desodiation among other electrodes. The Na-ion diffusion coefficient has been further calculated based on Equation (1).

$$D = R^2T^2 / 2A^2n^4F^4C^2\sigma^2_w \quad (1)$$

$$Z = R_e + R_{ct} + \sigma_w\,\omega^{-1/2} \quad (2)$$

herein, R is the universal gas constant (8.314 J mol^{-1} K^{-1}), T is the test temperature (298 K), F is the Faraday constant (96485 C mol^{-1}), n is the number of electrons transferred during the redox reaction, A is the active surface area of the electrode and C_0 is the concentration of sodium ions in the electrolyte (1 mol L^{-1}) [23]. According to Equation (2), σ_W is the Warburg factor and ω is the angular frequency, which is related to Z′ and can be attained from the slope of the fitting line of the EIS data (Fig. 4b **and** Fig. S7). Calculated $D_{(Na)}$ of $MoO_2@MoSe_2$/rGO electrode is 3.2×10^{-11} cm^2 s^{-1}, which is higher than that of $MoO_2@MoSe_2$ (2.3×10^{-12} cm^2 s^{-1}), $MoSe_2$/rGO (8.3×10^{-12} cm^2 s^{-1}) and $MoSe_2$ (1.8×10^{-12} cm^2 s^{-1}) counterparts.

To probe more kinetics information of the $MoO_2@MoSe_2$/rGO heterostructure electrode, a series of CV measurements at varied scan rates were recorded. Fig. 5a shows the CV profiles at 0.2–1.0 mV s^{-1} at a potential region of 0.01–3 V (vs. Na$^+$/Na). The CV curves exhibit similar peak shape and shift during both cathodic and anodic processes. Besides, some rectangle-like area could be easily discerned, suggesting a capacitive charge storage process [24]. The Na-ion transport kinetics in $MoO_2@MoSe_2$/rGO electrode could thus be mainly ascribed to a combination of diffusion-controlled and Faradaic-dominated processes. The capacity contribution can be evaluated using the power-law formula, $i = av^b$, which is based on the relationship between the peak current (i) and the scan rate (v) in the CV curves. The b-value can be obtained from the slope of the log(i)-log(v) plots [25]. In this equation, $b = 1.0$ suggests a capacitive process, while $b = 0.5$ represents a diffusion-controlled process. Fig. 5b shows the log(i)-log(v) plots in a wide potential range of both cathodic and anodic scans. As-calculated b values for the cathodic/anodic scans were all over 0.8, indicating that the fast kinetics were mainly governed by a surface induced capacitive process [26]. The fraction of pseudocapacitive contribution gradually improved by

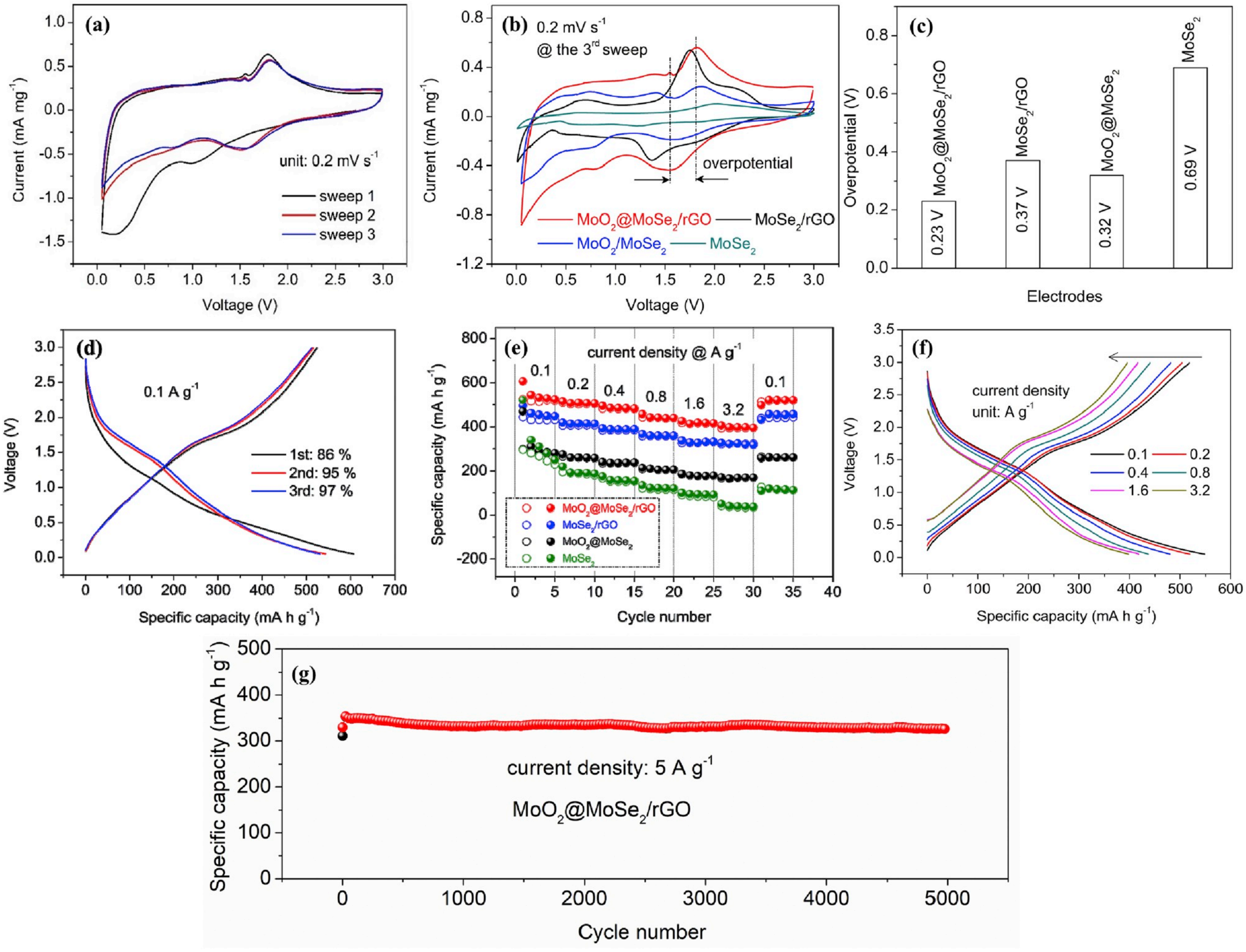

Figure 3. (a) CV curves of $MoSe_2@MoO_2/rGO$ for the first three cycles at a scanning rate of 0.2 mV s^{-1}; (b) CV curves at 3rd sweep of $MoSe_2@MoO_2/rGO$, $MoO_2@MoSe_2$, $MoSe_2/rGO$ and $MoSe_2$ for comparison; (c) Overpotentials among the electrodes calculated from redox peaks according to Fig. 3b; (d) Galvanostatic charge/discharge (GCD) curves of $MoSe_2@MoO_2/rGO$ measured at a current density of 0.1 A g^{-1}; (e) Rate capabilities at various current densities; (f) GCD curves of $MoO_2@MoSe_2/rGO$ at various current densities; (g) Long-term cycling performance of $MoO_2@MoSe_2/rGO$ at a current density of 5 A g^{-1}.

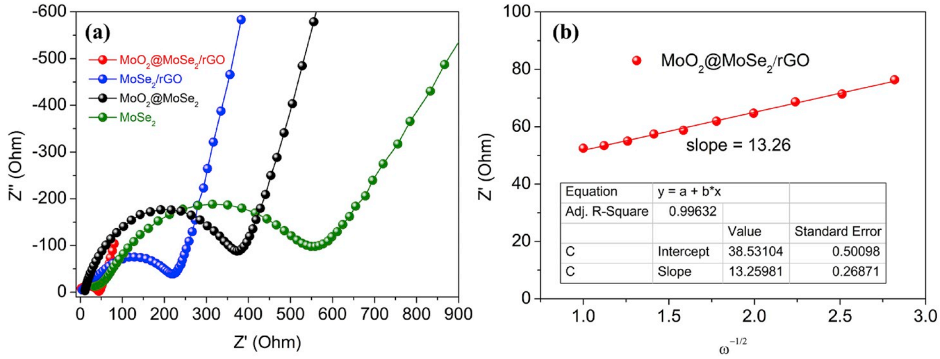

Equation	y = a + b*x	
Adj. R-Square	0.99632	
	Value	Standard Error
C Intercept	38.53104	0.50098
C Slope	13.25981	0.26871

Fig. 4. (a) The Nyquist plots after rate property test; (b) Z' as a function of $\omega^{-1/2}$ plot in low frequency range (slope: Warburg factor, σ_w).

increasing the scan rate (Fig. 5c) and reached a high of 86% and 98% under the sweep of 0.2 and 1.0 mV s^{-1}, respectively. The dominant capacitive-like process implies a fast sodiation/desodiation without obvious structural change, which agrees with the excellent rate capability and cycle stability.

First-principles density functional theory (DFT) calculations were next performed to gain more insight on the origin of high electronic/ionic conductivity in the $MoSe_2@MoO_2$ heterostructure. As demonstrated in previous works [9,10,14], the graphene can be pathways for electron transport and alleviate the volume changes, acting a novel "interface" between graphene and $MoSe_2$. Therefore, we mainly focus on the role of interface between $MoSe_2$ and MoO_2. Fig. 6a–d shows the crystal structure of $MoSe_2$ and MoO_2 after geometry optimization and corresponding density of states (DOS). The DOS region near the Fermi energy (E_f) level of MoO_2 is mainly composed of Mo-3d orbitals. The presence of abundant nonpolar Mo–Mo metallic bonds in MoO_2 and

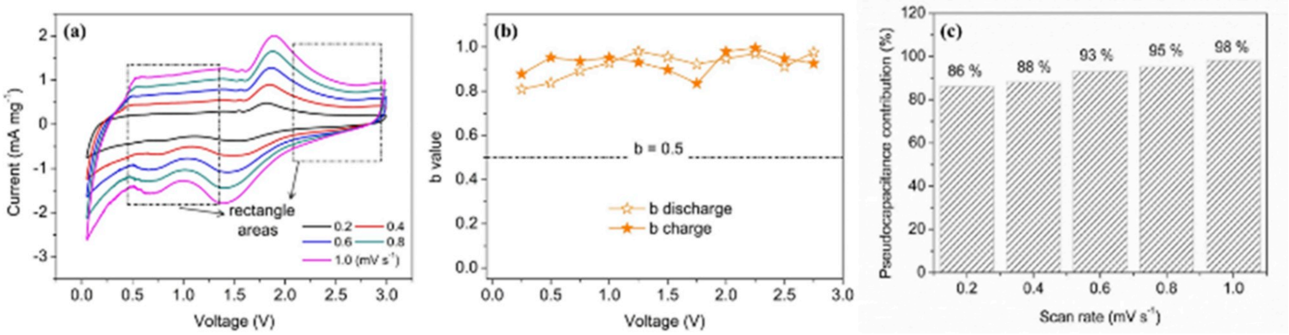

Fig. 5. (a) CV curves of $MoO_2@MoSe_2$/rGO at different scan rates. (b) Fitting the slope (b value) of scan rate and current of CV curves. (c) The capacitive contribution to charge storage at different scan rate of $MoO_2@MoSe_2$/rGO.

absence of an apparent bandgap suggest it's a metallic oxide with greatly enhanced electric conductivity [27]. In contrast, projected DOS (PDOS) of $MoSe_2$ reveals its semiconducting characteristic with a narrow bandgap of ~1 eV, and the Se 2p orbital and Mo 3d orbital contribute more to the valence band (VB) and conduction band (CB) regions, respectively. Interestingly, the DOS plots of the $MoSe_2@MoO_2$ (Fig. 6e and f) display metallic feature with diminished bandgap, suggesting that the decoration of MoO_2 nanoparticles on $MoSe_2$ sheets' surface effectively tuned the electronic structure of the resultant nanocomposites. Such modification can be mainly ascribed to the strong chemical coupling of $MoSe_2$ and MoO_2 components, leading to charge redistribution at heterointerface. The electron density distribution plot in Fig. 6g further reveals that some electrons have been transferred from MoO_2 to $MoSe_2$ at interface, together with formation of new Mo–Se bonds between MoO_2 and $MoSe_2$. These calculations result clearly illustrates that MoO_2 nanocrystals not only provide an integrative charge diffusion path but also provide abundant active sites for electron transfer, thus boosting the reaction kinetics.

The ultrahigh capacitive Na-ion storage capability of the $MoO_2@MoSe_2$/rGO anode promises it application in hybrid sodium ion capacitors (SICs). As a proof-of-concept, a SIC device was fabricated using $MoO_2@MoSe_2$/rGO as anode and activated carbon (AC) as cathode. The high specific surface area (1782 $m^2 g^{-1}$) and microporous characteristics (0.59 nm and 0.90 nm) of the AC (Figs. S8a–b) enable its fast Na-ion storage *via* an electric double layer capacitive (EDLC) mechanism proved by nearly linear GCD curves (Figs. S8c–d). The working principle of the as-prepared SIC is schematically illustrated in Fig. 7a. During the charge/discharge cycles, the ClO_4^- ions in the electrolyte were adsorbed and desorbed from the surface of the AC cathode while the Na-ions were adsorbed and intercalated into the $MoO_2@MoSe_2$/rGO anode [28]. The selection of the voltage window was aimed to achieve the best cyclic stability and energy density of the SICs while avoiding the irreversible side reactions in the electrolyte. The suitable working voltages have been optimized using CV curves at different voltage range (Fig. 7b). To avoid undesirable electrolyte decomposition and Na plating on the anode, 1 V has been chosen as the low cut-off potential [29]. With an increase in the operating potential window to 3.4 V, the current response increased. However, a higher upper cutoff potential of 3.6 V leads to side reaction [30]. Thus, an optimized operating potential window of 1.0–3.4 V was selected to further evaluate the overall electrochemical performance of SICs. The GCD test was performed to quantitatively evaluate the electrochemical performance of the device from 0.1 to 25.6 A g^{-1} (Fig. 7c). The asymmetric curves are typical of pseudocapacitive charge storage mechanism based on $MoO_2@MoSe_2$/rGO anode. The corresponding specific capacitances are 239 and 149 F g^{-1} at the current densities of 0.1 and 25.6 A g^{-1}, respectively (Fig. 7d). A high capacitance retention of 62% could be achieved when the current increases from 0.1 to 25.6 A g^{-1}, indicating an excellent rate capability of the SIC device. An excellent cyclic durability was also realized with a retention of 97% after 4500 charge/discharge cycles at a high current density of 10 A g^{-1} with high Coulombic efficiency of nearly 100%. The Ragone plot is shown in Fig. 7f. Compared with previously reported

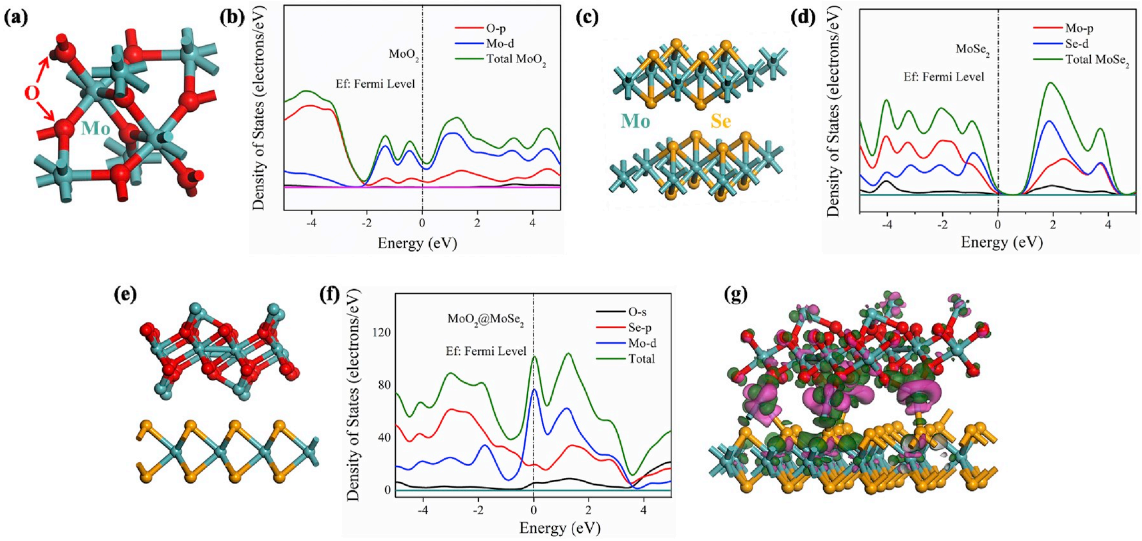

Fig. 6. Optimized geometry structures (a, c, e) and density of states (DOS; b, d, and f) contours of (a, b) MoO_2, (c, d) $MoSe_2$, and (e, f) $MoO_2@MoSe_2$ heterostructure. (g) Electron density difference map at the $MoSe_2@MoO_2$ heterointerface.

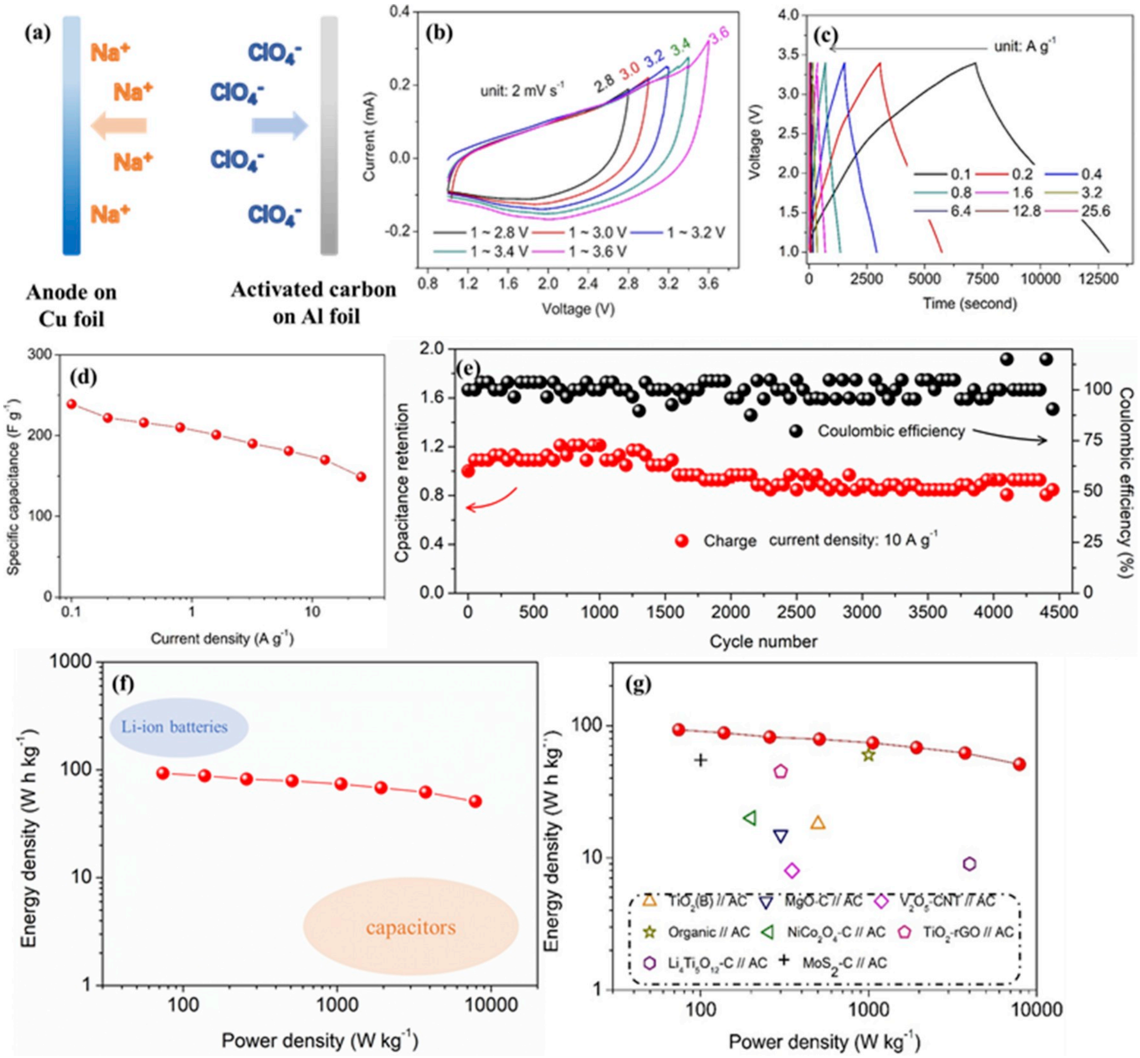

Fig. 7. (a) Schematic illustration of the charge-storage mechanisms for SICs based on MoO_2@$MoSe_2$/rGO anode; (b) CV curves of SICs measured at different potential windows at 2 mV s^{-1}; (c) Galvanostatic charge/discharge voltage profiles at different current densities between 1 V and 3.4 V; (d) Specific capacitances of SICs device at different current densities; (e) long-term cyclic performance of SIC at a current density of 10 A g^{-1} for 4500 cycles; Ragone plot (f) comparison of the SIC with other energy storage systems and (g) comparison of the SIC with literature reports.

SICs, as-prepared SIC device based on MoO_2@$MoSe_2$/rGO anode in this study can deliver an energy density of 51 W h kg^{-1} and a power output of 7920 W kg^{-1} at 12.8 A g^{-1}. Although the energy density is slightly lower than commercial Li-ion batteries, the simultaneous high power and high energy SIC device can bridge rechargeable batteries and supercapacitors as well as part of reported SIC systems (Fig. 7g **and** Table S2), filling the gap in the field of widely used energy storage systems.

4. Conclusion

Dual interface modified $MoSe_2$ (MoO_2@$MoSe_2$/rGO heterostructure) has been successfully synthesized and used as an anode for sodium ion batteries and capacitors. In such a hybrid, facilitated electron transport has been enhanced by the metallic MoO_2 and graphene. Enhanced sodium-ion diffusion has been realized in the heterostructure with the electronic coupling of metallic MoO_2 particles and ultrasmall $MoSe_2$ few-layered arrays chemically pinned on graphene. Charge accumulation between dual interface of MoO_2 and graphene around $MoSe_2$ further boosts the sodium-ion diffusion capabilities. Such structural merits endow the heterostructure composite with superior Na-storage capability in terms of high capacities, superior rate capabilities and long cyclabilities due to the enhanced electron and Na-ion transport at interface as well as superior structural stability. When further applied in hybrid sodium ion capacitors with activated carbon cathode, the device exhibits prolonged cycling life at 10 A g^{-1} with a capacitance retention over 97% after 4500 cycles. Notably, the energy densities and powder outputs of as-assembled MoO_2@$MoSe_2$/rGO//AC SICs reach more than 51 W h kg^{-1} and 7920 W kg^{-1}. This work can provide new insights into the rational engineering and exploration of advanced state-of-the-art anode materials for high performance sodium-ion storage applications.

Acknowledgements

This work was supported by the National Science Foundation (NSF-CBET No. 1803256) and National Natural Science Foundation of China (No. 51804089 and 51875232). Part of this work was conducted at the Molecular Analysis Facility supported in part by the National Science Foundation (grant ECC-1542101) and the Clean Energy Institute at the University of Washington. H.-E. Wang thanks the support of "Chutian Scholar" in Hubei Provincial Department.

Appendix A. Supplementary data

Supplementary data to this article can be found online at https://doi.org/10.1016/j.jpowsour.2019.227298.

References

[1] R.C. Massé, E. Uchaker, G. Cao, Beyond Li-ion: electrode materials for sodium- and magnesium-ion batteries, Sci. China. Mater. 58 (2015) 715–766.

[2] Z. Shadike, E. Zhao, Y. Zhou, X. Yu, Y. Yang, E. Hu, S. Bak, L. Gu, X. Yang, Advanced characterization techniques for sodium-ion battery studies, Adv. Energy Mater. (2018), 1702588.

[3] F. Li, Z. Zhou, Micro/nanostructured materials for sodium ion batteries and capacitors, Small 14 (2018), 1702961.

[4] Y. Liu, N. Zhang, L. Jiao, Z. Tao, J. Chen, Ultrasmall Sn nanoparticles embedded in carbon as high-performance anode for sodium-ion batteries, Adv. Funct. Mater. 25 (2015) 214–220.

[5] J. Zhang, W. Lv, D. Zheng, Q. Liang, D. Wang, F. Kang, Q. Yang, The interplay of oxygen functional groups and folded texture in densified graphene electrodes for compact sodium-ion capacitors, Adv. Energy Mater. 8 (2018), 1702395.

[6] D. Xu, D. Chao, H. Wang, Y. Gong, R. Wang, B. He, X. Hu, H.J. Fan, Flexible quasi-solid-state sodium-ion capacitors developed using 2D metal-organic-framework array as reactor, Adv. Energy Mater. 8 (2018), 1702769.

[7] D. Sun, D. Ye, P. Liu, Y. Tang, J. Guo, L. Wang, H. Wang, MoS_2/Graphene nanosheets from commercial bulky MoS_2 and graphite as anode materials for high rate sodium-ion batteries, Adv. Energy Mater. 8 (2018), 1702383.

[8] X. Liu, Y. Hao, J. Shu, H.M.K. Sari, L. Lin, H. Kou, J. Li, W. Liu, B. Yan, D. Li, J. Zhang, X. Li, Nitrogen sulfur dual-doping of reduced graphene oxide harvesting hollow $ZnSnS_3$ nano-microcubes with superior sodium storage, Nano Energy 57 (2019) 414–423.

[9] G. Li, D. Luo, X. Wang, M.H. Seo, S. Hemmati, A. Yu, Z. Chen, Enhanced reversible sodium-ion intercalation by synergistic coupling of few-layered MoS_2 and S-doped graphene, Adv. Funct. Mater. 27 (2017), 1702562.

[10] X. Wang, G. Li, M.H. Seo, F.M. Hassan, M.A. Hoque, Z. Chen, Sulfur atoms bridging few-layered MoS_2 with S-doped graphene enable highly robust anode for lithium-ion batteries, Adv. Energy Mater. 5 (2015), 1501106.

[11] M. Zhu, Z. Luo, A. Pan, H. Yang, T. Zhu, S. Liang, G. Cao, N-doped one-dimensional carbonaceous backbones supported $MoSe_2$ nanosheets as superior electrodes for energy storage and conversion, Chem. Eng. J. 334 (2018) 2190–2200.

[12] H. Liu, H. Guo, B. Liu, M. Liang, Z. Lv, K.R. Adair, X. Sun, Few-layer $MoSe_2$ nanosheets with expanded (002) planes confined in hollow carbon nanospheres for ultrahigh-performance Na-ion batteries, Adv. Funct. Mater. 28 (2018), 1707480.

[13] Z. Wang, T. Chen, W. Chen, K. Chang, L. Ma, G. Huang, D. Chen, J.Y. Lee, CTAB-assisted synthesis of single-layer MoS_2-graphene composites as anode materials of Li-ion batteries, J. Mater. Chem. A 1 (2013) 2202–2210.

[14] Y. Cai, H. Wang, X. Zhao, F. Huang, C. Wang, Z. Deng, Y. Li, G. Cao, B. Su, Walnut-like porous core/shell TiO_2 with hybridized phases enabling fast and stable lithium storage, ACS Appl. Mater. Interfaces 9 (2017) 10652–10663.

[15] Z. Luo, J. Zhou, L. Wang, G. Fang, A. Pan, S. Liang, Two-dimensional hybrid nanosheets of few layered $MoSe_2$ on reduced graphene oxide as anodes for long-cycle-life lithium-ion batteries, J. Mater. Chem. A 4 (2016) 15302–15308.

[16] Y. Sun, X. Hu, J.C. Yu, Q. Li, W. Luo, L. Yuan, W. Zhang, Y. Huang, Morphosynthesis of a hierarchical MoO_2 nanoarchitecture as a binder-free anode for lithium-ion batteries, Energy Environ. Sci. 4 (2011) 2870.

[17] Y. Sun, X. Hu, W. Luo, Y. Huang, Self-assembled hierarchical MoO_2/graphene nanoarchitectures and their application as a high-performance anode material for lithium-ion batteries, ACS Nano 5 (2011) 7100–7107.

[18] Y. Ding, P. Kopold, K. Hahn, P.A. Van Aken, J. Maier, Y. Yu, A lamellar hybrid assembled from metal disulfide nanowall arrays anchored on a carbon layer: in situ hybridization and improved sodium storage, Adv. Mater. 28 (2016) 7774–7782.

[19] C. Xia, Y. Zhou, D.B. Velusamy, A.A. Farah, P. Li, Q. Jiang, I.N. Odeh, Z. Wang, X. Zhang, H.N. Alshareef, Anomalous Li storage capability in atomically thin two-dimensional sheets of nonlayered MoO_2, Nano Lett. 18 (2018) 1506–1515.

[20] H. Liu, B. Liu, H. Guo, M. Liang, Y. Zhang, T. Borjigin, X. Yang, L. Wang, X. Sun, N-doped C-encapsulated scale-like yolk-shell frame assembled by expanded planes few-layer $MoSe_2$ for enhanced performance in sodium-ion batteries, Nano Energy 51 (2018) 639–648.

[21] G. Jia, H. Wang, D. Chao, H. He, H.T. Nguyen, Y. Zhang, Z. Zhang, H.J. Fan, Ultrathin $MoSe_2$@N-doped carbon composite nanospheres for stable Na-ion storage, Nanotechnology 28 (2017).

[22] H. Wang, X. Zhao, X. Li, Z. Wang, C. Liu, Z. Lu, W. Zhang, G. Cao, rGO/SnS_2/TiO_2 heterostructured composite with dual-confinement for enhanced lithium-ion storage, J. Mater. Chem. A 5 (2017) 25056–25063.

[23] Z. Zhang, M. Li, Y. Gao, Z. Wei, M. Zhang, C. Wang, Y. Zeng, B. Zou, G. Chen, F. Du, Fast potassium storage in hierarchical $Ca_{0.5}Ti_2(PO_4)_3$@C microspheres enabling high-performance potassium-ion capacitors, Adv. Funct. Mater. (2018), 1802684.

[24] X. Yang, R. Zhang, J. Zhao, Z. Wei, D. Wang, X. Bie, Y. Gao, J. Wang, F. Du, G. Chen, Amorphous tin-based composite oxide: a high-rate and ultralong-life sodium-ion-storage, Material. Adv. Energy Mater. 8 (2018), 17018278.

[25] D. Chao, C.M. Lai, P. Liang, Q. Wei, Y. Wang, C.R. Zhu, G. Deng, V.V.T. Doan-Nguyen, J. Lin, L. Mai, H.J. Fan, B. Dunn, Z.X. Shen, Sodium vanadium fluorophosphates (NVOPF) array cathode designed for high-rate full sodium ion storage device, Adv. Energy Mater. 8 (2018), 1800058.

[26] G.A. Muller, J.B. Cook, H. Kim, S.H. Tolbert, B. Dunn, High performance pseudocapacitor based on 2D layered metal chalcogenide nanocrystals, Nano Lett. 15 (2015) 1911–1917.

[27] J. Hao, J. Zhang, G. Xia, Y. Liu, Y. Zheng, W. Zhang, Y. Tang, W.K. Pang, Z. Guo, Heterostructure manipulationvia in situ localized phase transformation for high-rate and highly durable lithium ion storage, ACS Nano 12 (2018) 10430–10438.

[28] J. Zhao, G. Wang, R. Hu, K. Zhu, K. Cheng, K. Ye, D. Cao, Z. Fan, Ultrasmall-sized SnS nanosheets vertically aligned on carbon microtubes for sodium-ion capacitors with high energy density, J. Mater. Chem. A 7 (2019) 4047–4054.

[29] L. Shen, H. Lv, S. Chen, P. Kopold, P.A. van Aken, X. Wu, J. Maier, Y. Yu, Peapod-like Li_3VO_4/N-doped carbon nanowires with pseudocapacitive properties as advanced materials for high-energy lithium-ion capacitors, Adv. Mater. 29 (2017), 1700142.

[30] C. Liu, C. Zhang, H. Fu, X. Nan, G. Cao, Exploiting high-performance anode through tuning the character of chemical bonds for Li-ion batteries and capacitors, Adv. Energy Mater. 7 (2017), 1601127.